

The influence of double pulse delay and ambient pressure on femtosecond laser ablation of silicon

Ying Qi, Hongxia Qi, Qinxin Wang, Zhou Chen, Zhan Hu*

Institute of Atomic and Molecular Physics, Jilin University, Changchun 130012, People's Republic of China

ARTICLE INFO

Article history:

Received 7 April 2014
Received in revised form
8 June 2014
Accepted 21 June 2014

Keywords:

Femtosecond double pulse
Ablation
Morphology

ABSTRACT

The effects of double pulse delay time and ambient pressure on femtosecond laser ablation of Si are studied by means of photoluminescence and morphology analysis. Detailed scan of double pulse delay is performed at vacuum (2 Pa) and atmospheric pressure, and detailed scan of pressure is performed at three double pulse delay times of 0.2 ps, 53.13 ps and 106.47 ps. It is found that, at various fluences, photoluminescence intensity and morphology change as functions of both double pulse delay and ambient pressure. Especially, the shape of the splashing droplets also changes at different experimental conditions, indicating higher or lower sample temperature. The observations are explained by the efficiently energy coupling between the second pulse and the liquid layer produced by the first one, and the pressure dependent energy coupling between plasma and liquid phase as well as ambient gas.

© 2014 Elsevier Ltd. All rights reserved.

1. Introduction

Laser ablation of material is a complex process involving several phases and multiple length and time scales [1–3]. A sequence of different events is initiated after the laser irradiation. The type and order of these events are determined by the properties of the material and the laser [4,5]. Micromachining with laser pulses of femtosecond width has been shown to limit the amount of thermal diffusion due to the very short heating duration and the rapid solid-to-vapor phase transition. The absorption region is limited to penetration depth of the optical pulse; thus collateral damage is limited.

Double pulses have been used to probe or control the ablation mechanisms, such as energy deposition, heat transfer, material removal processes in various materials of metal, semiconductor or dielectrics [6–8]. It is shown that photoluminescence emission during ablation is enhanced when the double pulse delay, defined as the time between two sub-pulses, is set to a few tens of picoseconds [6,7]. Compared with nanosecond and picosecond laser pulses, the plasma reheating effect can be ignored in the femtosecond single pulse ablation process [9–13]. However, with femtosecond double pulses, plasma reheating does show some effect. For example, at the fluence of 15.1 J/cm², in copper ablation experiments [14], it is observed that the plasma luminosity increases with double pulse delay, while the ablation depth decreases. These results reveal that the interaction of laser–plasma plays a prominent role during the whole ablation process, and the results are in qualitative agreement with the

simulation result described in Ref. [15]. With the laser fluences of 1.6 kJ/cm² and 1.2 kJ/cm², maximum enhancement of ion density and average ion energy in ablation plume of silicon is observed at the double pulse delay time of 5 ps [16,17]. The results are explained by the appropriate plasma density gradient with a properly positioned critical surface, which interacts most strongly with the second pulse.

The effect of the surrounding gas and pressure on laser ablation of solid sample has received much increased attention in recent years because of its importance in pulsed laser deposition [18], nanoparticle formation and growth [19], laser micromachining [20], and laser-induced breakdown spectroscopy (LIBS) [21]. After the irradiation of the surface of solid sample by high powered laser pulse, the produced plasma expands as a shock wave into the surrounding atmosphere at supersonic speed. The energy of plasma transfers into the environment gas through several processes [22,23], such as shock wave heating, thermal conduction, radiative emission, and ion recombination. The selection among these interaction processes depends on the pulse energy, pulse duration, laser wavelength, as well as composition and condition of environment gas. With nanosecond laser pulse, Lobe et al. studied the influence of the environment gas and gas mixture on the ablation of steel [24]. The ablation efficiency can be increased not only by increasing the laser fluence, but also by changing the ambient pressure. The results are attributed to the enhanced interaction between the plasma and the sample in certain ambient gas pressure. Bashir et al. [25,26] analyzed the influence of the different gases at the different pressures on optical emission intensity, electron temperature and density. It is revealed that nanosecond LIBS performance is strongly affected by the ambient condition due to the shielding effect of plasma. For femtosecond laser ablation [27–29], at a certain background air pressure (around 500 Pa), the photoluminescence intensity

* Corresponding author.

E-mail address: huzhan@jlu.edu.cn (Z. Hu).

can be significantly enhanced compared with the atmospheric pressure, which is attributed to the further expansion of plasma into ambient gas and not being cooled as rapidly by the surrounding species. While at low pressure condition (around 0.4 Pa), the decreased emission intensity is due to the decreased collisional excitation and less energy transmission between the plasma and the surrounding gas particle. In addition, more thermal energy is retained in sample under gas environment, compared to lower pressure condition as reported in [30–32], because the high-pressure plasma can affect the coupling of the thermal energy with the sample. The explanations of the results are based on two mechanisms: a certain amount of the laser energy stored in the plasma can be transferred to the sample surface; compared with vacuum condition, the increased redeposition of the ablated material at higher gas pressure enhanced the thermal energy coupling to the sample. In order to explain the enhancement of retained thermal energy in a gas environment, a combined model is developed to simulate the ablation process, which is based on 2D thermal model of laser-induced heating and ambient gas dynamics [33]. The simulation shows that the hot plasma moves preferentially toward the sample and its thermal energy couples efficiently with the sample. Time-resolved pump-probe shadow graphic imaging results also show that the ambient air assisted in dissipating the energy into the sample [34].

Silicon and its compounds are widely used in semiconductor industries, the properties of which and their interaction mechanisms with external fields have been the study subject of many experimental as well as theoretical works [35–37]. The interaction of Si with laser has received more and more interest [38,39]. In our previous studies [6,7], we also used Si as the sample, which is ablated by femtosecond double pulse at very low fluences and atmospheric pressure. It was found that, with increasing double pulse delay, photoluminescence intensity increases monotonically. However, the enhancement ratio of photoluminescence intensity at longer double pulse delay to that at shorter delay will decrease, with increasing fluence. The ablation behavior under higher laser fluence will be studied in this paper. It was also observed in our previous work that, with increasing double pulse delay, the amount of resolidified liquid material increases. However, the crater volume does not change much with double pulse delay, which was attributed to the redeposition of materials back into the crater. Under lower environment pressure condition, the behavior of ejected material may be quite different. So the study of ablation under different environment pressure conditions is important.

In this paper, in order to further reveal the mechanisms of femtosecond laser interaction with materials, we investigate systematically the ablation of Si with double femtosecond laser pulses. At different double pulse delays and ambient pressure values, besides photoluminescence intensity, the morphology of ablation craters (including splashing droplet shape, crater depth, width and volume) is studied, which was not reported in other works. Especially, we do careful analysis of the splashing droplet shape and show that the shape changes under different experimental conditions, which reflects the ablation mechanisms. A complete scan of all double pulse delays and pressure values is not possible. We do detailed double pulse delay scans at vacuum condition (2 Pa) and atmospheric pressure, which will be discussed in Section 3.1; and then do detailed pressure scans at three double pulse delay values of 0.2 ps, 53.13 ps, and 106.47 ps, which will be discussed in Section 3.2.

2. Experimental

The experimental setup used in this paper is similar to that described in Ref. [6], as shown in the schematic drawing in Fig. 1, which consists of a femtosecond laser source, a Michelson interferometer to generate double pulse with a controllable delay, a sample manipulator, and an optical detector. A regenerative amplifier laser

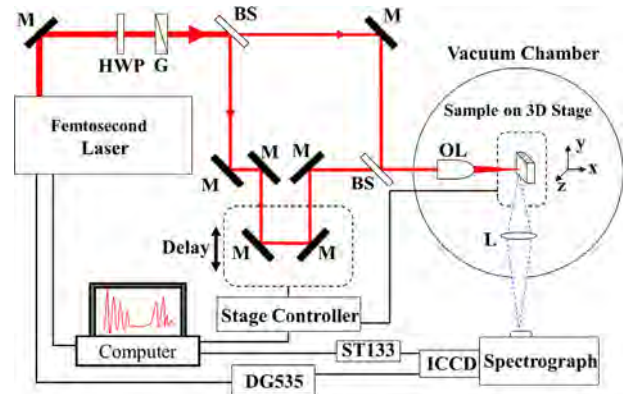


Fig. 1. Schematic drawing of the experimental setup. The setup can be divided into four parts: laser, laser beam manipulation, vacuum chamber, control and data acquisition. Laser beam manipulation components include half-wave plate (HWP), Glan prism (G), beam splitters (BS), high reflective mirrors (M), and microscope objective lens (OL). Control and data acquisition components include 1D (Delay) and 3D stages, lens (L), stage controller, DG535 delay generator, ST133 camera controller, intensified CCD camera (ICCD), spectrograph, and computer.

system (Spectra Physics Tsunami oscillator and Spitfire amplifier) producing 800 nm, 110 fs (FWHM) pulses at a repetition rate of 1 kHz with pulse energy up to ~ 0.7 mJ is used. Laser energy is varied by adjusting the half-wave plate followed by a Glan prism. The laser is then divided into two beams and later combined into one beam in a Michelson interferometer setup, in which the optical length of one beam can be adjusted, resulting in a varying double pulse delay from -53.53 ps to 106.47 ps. For all the experiments the intensities of the two pulses are equal. The overlapped pulses are focused onto the sample by a $10\times$ objective lens (Edmund Optic, NT59-877) with a numerical aperture of 0.28, and working distance of 33.5 mm. The focus size is measured using a moving knife-edge method [40] to be $0.97\ \mu\text{m}$ in diameter, which results in $135\ \text{J}/\text{cm}^2$ fluence with a $1\ \mu\text{J}$ pulse energy. The sample is undoped Si (111) wafer (MTI Crystal), which is mounted on a motorized XYZ high precision translation stage (Newport, M-462-XYZ-SD stage and TRA25cc actuators) in a vacuum chamber. The sample's normal axis is at an angle of 30° with respect to the laser beam direction. The laser is operated in single shot mode and the stage moves the sample to a new location after each laser spot. Photoluminescence perpendicular to the laser beam is collected by an $f/2.0$ lens, focused into a spectrograph (Princeton Instruments, PI Acton SP500i) and detected by an ICCD detector (PI-MAX, 1024×256 pixel). The ICCD is operated in shutter mode with an exposure time of 100 ms which is long enough to collect any photoluminescence generated. The spectrum intensity at all wavelengths in the spectrum range studied (350–600 nm) follows the same trend as a function of double pulse delay. So in this work, the strongest Si^+ emission line at 505.6 nm, from $3s^2 4p(^2P_{3/2}) \leftarrow 3s^2 4d(^2D_{5/2})$ transition, is measured. An average of typically 25 shots is taken for each data point. When we investigate the effect of ambient pressure during the ablation process, air is used as buffer gas. The morphology of the ablated crater is measured by an Atomic Force Microscope (AFM, BenYuan, CSPM5500) operated in contact mode. The maximum lateral resolution and vertical resolution of AFM are 0.2 nm and 0.01 nm, respectively. The scanning range is $50 \times 50\ \mu\text{m}$.

3. Results and discussion

3.1. Double pulse ablation of Si with different delay values and laser fluences in vacuum and atmospheric pressure

First, we ablate the Si sample in vacuum (2 Pa) and atmospheric condition with different laser fluences and double pulse delays. The photoluminescence obtained in atmospheric condition and in

vacuum is of different intensities (which will be discussed in Section 3.2), but follows same trends, so only data obtained in vacuum condition are plotted. As shown in Fig. 2, the photoluminescence emission intensity is found to increase with a monotonic trend with double pulse delay at the lowest fluences, 40.6 J/cm² and 135 J/cm², which is consistent with the result obtained in our previous double pulse experiments in air [6,7]. The small photoluminescence intensity peaks observed at about 30 ps for 40.6 J/cm² and about 5 ps for 135 J/cm² are caused by fluctuations of the photoluminescence intensity because of experimental uncertainties, for example the random shape of generated plasma and thus the influenced interaction of the plasma with the second pulse. In order to avoid the interference of two pulses at exact zero delay, the delay time of the point closest to zero delay is set to 0.2 ps. A liquid layer is created after the first pulse irradiates the sample, in the case of Si sample, the metallic liquid absorbs more laser energy compared with the weak absorbing solid [41,42]. With increasing double pulse delay, the solid–liquid phase front propagates further into the bulk material, the liquid layer generated by the first pulse absorbs energy more efficiently than the solid, producing a higher energy density and therefore higher temperatures within the material [43,44]. These higher temperatures will then cause an increase in both the amount of material removed

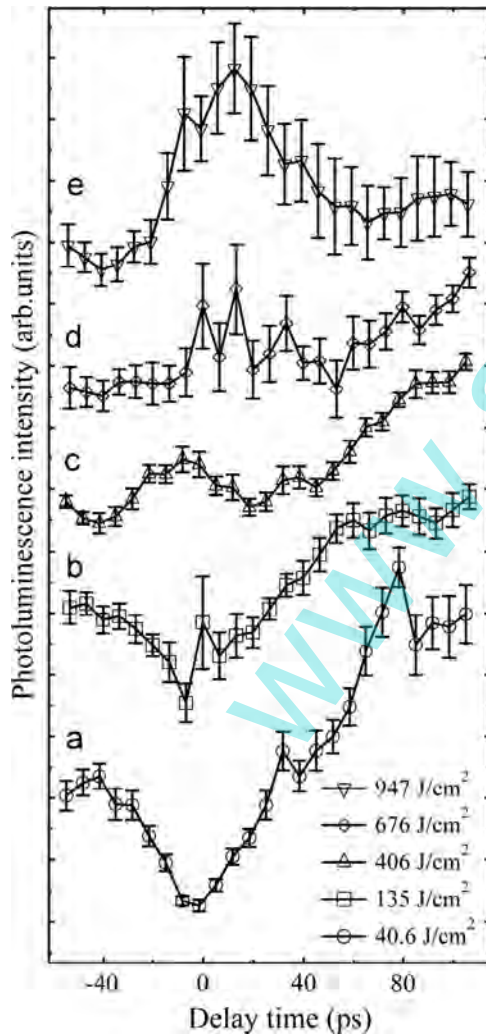


Fig. 2. Photoluminescence intensity from Si(111) at 505.6 nm as a function of femtosecond double pulse delay, with different laser fluences of (a) 40.6 J/cm², (b) 135 J/cm², (c) 406 J/cm², (d) 676 J/cm² and (e) 947 J/cm². Different curves are obtained with different gain of the ICCD detector and the intensities between them are not comparable.

and the concentration of excited species, giving an enhancement of the photoluminescence. Compared with single pulse, at low laser fluence, double pulse irradiation produces clean and smooth structures on the surface of silicon, which is shown by a scanning electron microscope image of the crater in Ref. [45]. This is an obvious evidence for the second pulse coupling with a molten layer [46]. However, when the laser fluence is in the range of 405–947 J/cm², with the increase of double pulse delay, the emission intensity will decrease initially, reach a minimum at certain delay time, then start to increase. The oscillation of data and offset of maximum from zero delay are caused by fluctuations of the measured photoluminescence intensity. When the double pulse delay is close to 0 ps, the second pulse is absorbed strongly by the free electron produced from the first one through the mechanism of Inverse Bremsstrahlung (IB) [4]. The overall intensity of photoluminescence, including the background Bremsstrahlung continuum, increases because of the interaction between high-energy electrons and atoms or ions [47]. As the double pulse delay increases, significant expansion of free electrons reduces the electron density in laser–sample interaction region, and weakens the absorption of the second pulse by the electrons. The maximum of electron and ion density has been observed at delay time of 5 ps, after which the density decreases with increasing double pulse delay [16]. The overall emission intensity will decrease because of the weaker collisions between electrons and other particles. When double pulse delay increases to a certain value, the plasma density becomes low enough so that the second pulse can penetrate and irradiate on the liquid phase formed by the first pulse. The stronger energy coupling thus enhances the emission intensity [6,7,43–45].

Next, we study the morphology of ablation craters by using AFM. Fig. 3(a), (b), (e) and (f) shows some typical AFM images at two different fluences and two double pulse delays of 0.2 ps and 106.47 ps in vacuum. The crater obtained with fluence of 40.6 J/cm² has clear contour and smooth rim (Fig. 3(a) and (e)). Increasing the delay time, the contour becomes a little irregular and some structures appear on the rim (as seen in Fig. 3(e)). At the laser fluences of 405 J/cm² (Fig. 3(b) and (f)), a large portion of splashing materials redeposits around the ablation craters as droplets, which are shown by the solid line arrow. At the double pulse delay of 106.47 ps (Fig. 3(f)), compared with the delay of 0.2 ps (Fig. 3(b)), we can see more clear tails following the droplets, which are shown by the dashed line arrow in Fig. 3. The tails are short and not clear at the double pulse delay of 0.2 ps. And, the size of droplets with the delay of 0.2 ps is significantly different from that of 106.47 ps with the same laser fluence. In Fig. 4, the cross sections of the droplets selected randomly from the AFM images for four different laser fluences are presented. At 106.47 ps, the height of droplet is obviously greater than that at 0.2 ps. The evolution of the height and width of the droplets is illustrated in Fig. 5, as functions of four double pulse delays. The data from ten droplets around a crater are averaged. The height is much smaller than the width, and the shape of the droplet is more like a thin slab, when double pulse delay is shorter (0.2 ps). At longer time delay (106.47 ps), the shape becomes more congregated, where the droplet width decreases, while the height increases. After the irradiation of laser pulse, the sample will be in a mixed phase of liquid and solid. Compared with shorter time delay, with longer delayed double pulse, because of better coupling of laser pulse and liquid phase created by the first pulse [6,7,43–45], the energy density in the irradiated sample is high, resulting in high temperature and larger ratio of liquid phase to solid phase. In this higher temperature mixture, the size of solid phase pieces will be smaller compared to that in lower temperature mixture. Hence, the ejected droplets will contain smaller portion of solid phase covered by larger portion of liquid phase. Because of surface tension of the

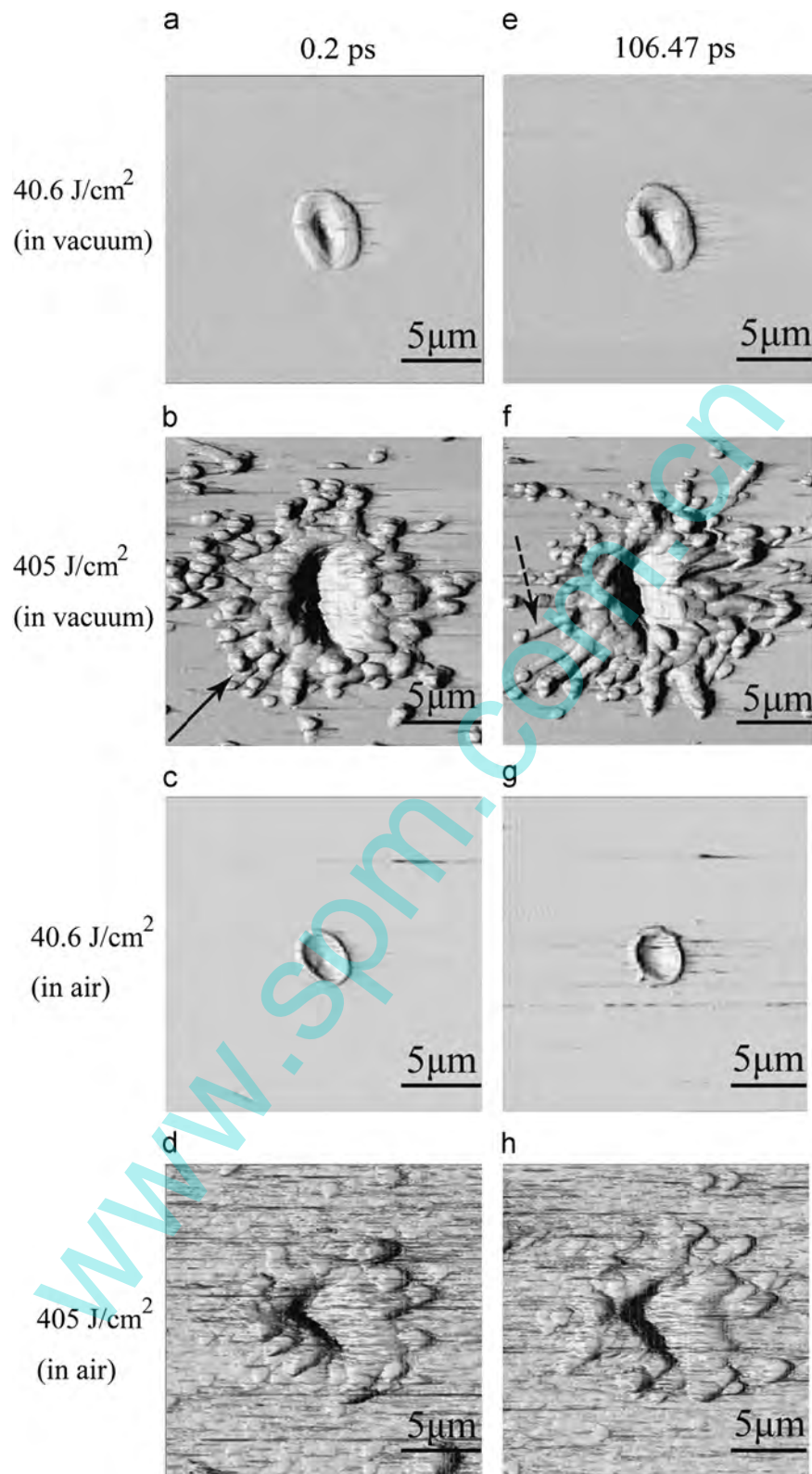


Fig. 3. AFM images of ablated craters in vacuum (a, b, e, and f) and in atmospheric pressure (c, d, g, and h). The laser fluences are 40.6 J/cm^2 (a, e, c, and g) and 405 J/cm^2 (b, f, d, and h). Double pulse delays are 0.2 ps (left column) and 106.47 ps (right column). The splashing material as droplet is shown by the solid line arrow, the tail is shown by the dashed line arrow.

liquid phase, the droplets will tend to form round shape. Thus, we observe droplets with smaller width to height ratio at longer double pulse delay. Moreover, after absorbing energy of the second pulse, homogeneous melting is followed by rapid expansion of the superheated mixed phase material, the system is readily driven into the

liquid–vapor coexistence state which initiates phase explosion [48,49]. The ejected liquid material then cools rapidly and resolidifies, leaving behind more radial structures as tails following the droplets. Both the shape change and appearance of tails indicate higher degree of melting at longer double pulse delay, because of

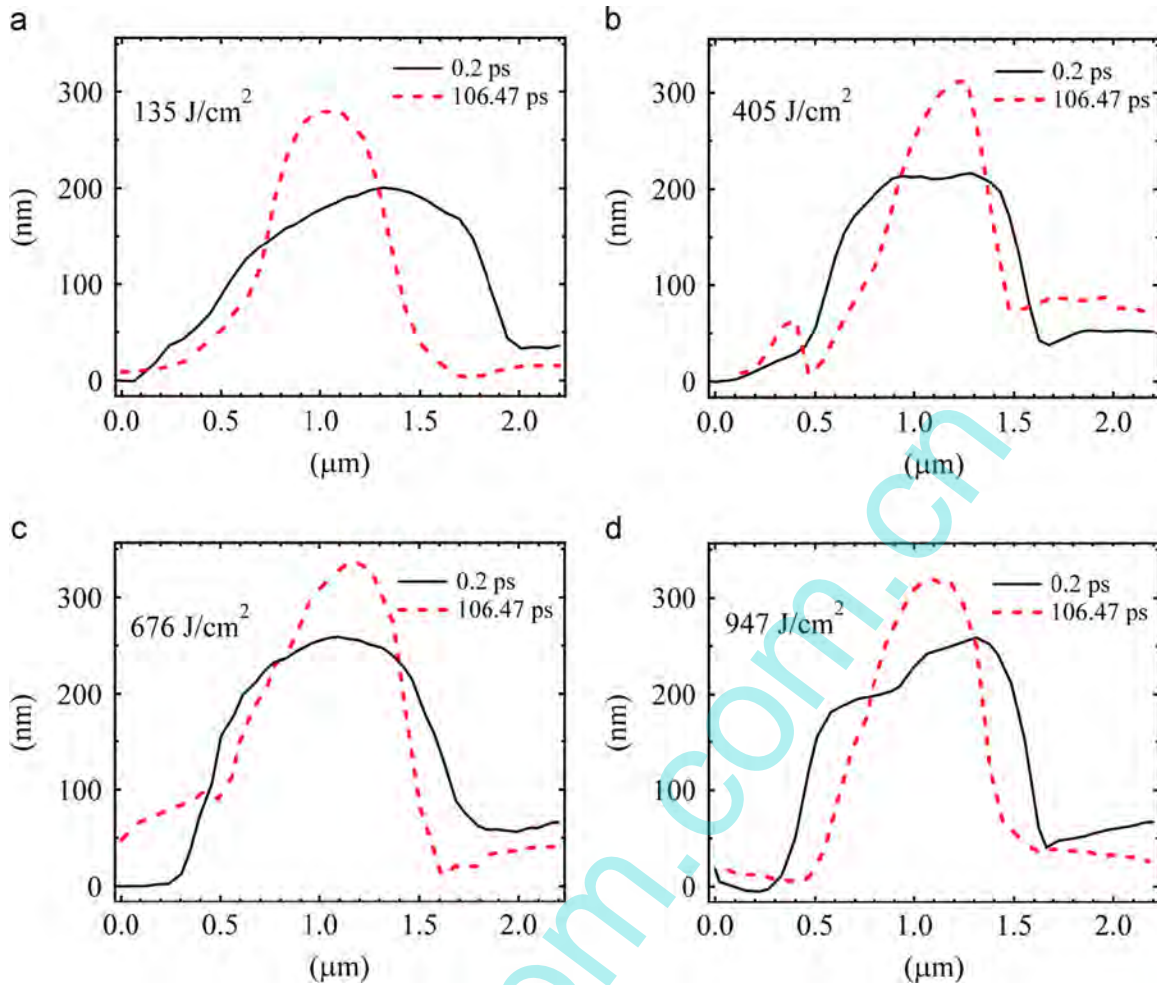


Fig. 4. AFM cross sections for droplets obtained at double pulse delays of 0.2 ps (black solid line) and 106.47 ps (red dash line), with laser fluence of (a) 135 J/cm², (b) 405 J/cm², (c) 676 J/cm² and (d) 947 J/cm². (For interpretation of the references to color in this figure legend, the reader is referred to the web version of this article.)

the stronger interaction between the second pulse and the silicon liquid phase. At the same time, this stronger absorption of energy from the second pulse also results in higher photoluminescence emission, as seen in Fig. 2(a)–(d).

Fig. 3(c), (d), (g) and (h) shows some typical AFM images at two laser fluences and two double pulse delays of 0.2 ps and 106.47 ps in atmospheric pressure. With fluence of 40.6 J/cm², at longer double pulse delay (compare Fig. 3(c) and (g)), some tiny particles can be observed to redeposit around the crater. As the fluence increases to 405 J/cm² (Fig. 3(d) and (h)), more quantity of tiny particles redeposit on the sample surface, resulting in the blurred AFM image. Due to the stronger confinement effect of environment gas under atmospheric pressure, compared to lower pressure condition, more quantity of ejected materials during ablation will redeposit back around the crater. It is difficult to study droplet shape as a function of double pulse delay with the blurred image. The differences of morphology of craters obtained with the same fluence but under different pressures will be discussed in the next section.

3.2. Ablation of Si under different ambient pressures

In the next experiment, the sample is ablated with a low laser fluence of 40.6 J/cm² and a high fluence of 676 J/cm², environment pressure is scanned from 2 Pa to atmospheric pressure, photoluminescence intensity is recorded at three double pulse delays, 0.2 ps, 53.13 ps and 106.47 ps. Firstly, the increase and decrease of

the photoluminescence intensity and crater dimension are caused by the competition of two mechanisms, i.e. plasma interaction with the sample and plasma interaction with environmental gas, as discussed in detail in the following paragraphs. These mechanisms exist in higher fluence of 676 J/cm² as well as in lower fluence of 40.6 J/cm². So the photoluminescence intensity and crater dimension as functions of pressure obtained at two fluences follow similar trends. Thus, only data obtained at 676 J/cm² are depicted in Fig. 6. Secondly, from the morphology, i.e. crater depth, width and volume, in Fig. 6, the ambient pressure effect on ablation is independent of double pulse delay. Therefore, only data obtained at 0.2 ps are shown in Fig. 7–9.

As shown in Fig. 6(a), with increasing pressure, the photoluminescence intensity increases and reaches maxima at around 10³ Pa, decreases in even higher pressure region, with a slight increase at atmospheric pressure. The higher degree of plasma expansion in the low pressure condition results in lower electron density and temperature within the plasma. The weak interaction, including thermal energy coupling and pressure between the plasma and the sample surface, hence less energy transferred to sample surface, results in relatively low emission intensity [30–32]. When the ambient pressure is in the range of 2–10³ Pa, the increasing pressure of the ambient gas can restrain the expansion of the ablated material, which enhances the thermal coupling to the sample due to an increased redeposition of the ablated material compared with the vacuum condition [30–32]. On the other hand, the expansion of plasma is restricted too, i.e. the confinement effect

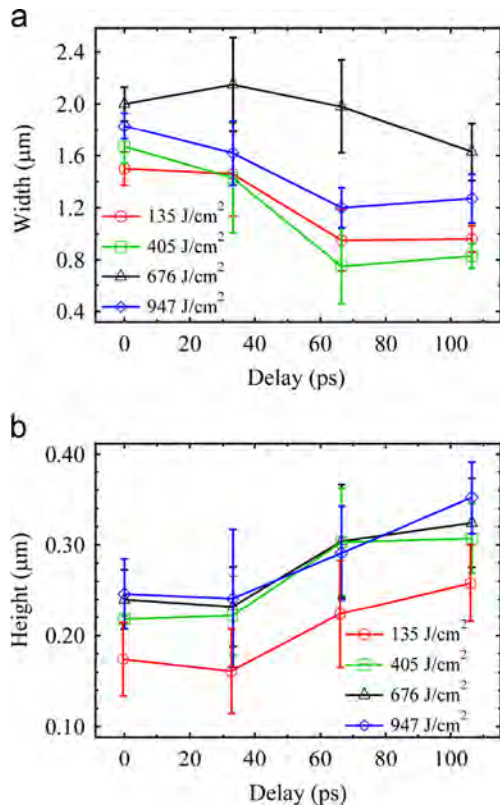


Fig. 5. (a) Average width and (b) height of droplets around the crater as functions of femtosecond double pulse delay, with laser fluences of 135 J/cm^2 (red circle), 405 J/cm^2 (green square), 676 J/cm^2 (black triangle) and 947 J/cm^2 (blue diamond), an average from 10 droplets is taken for each data point. (For interpretation of the references to color in this figure legend, the reader is referred to the web version of this article.)

of plasma assists ablation [25]. At higher pressure in the range of 10^3 Pa to atmospheric pressure, the effective frequency of electron elastic and inelastic collisions with the surrounding gas particle increases [21,26]. The predominant non-adiabatic process delivers more plasma energy to the surrounding gas particle. The decrease of electron density and temperature weakens the energy coupling between the plasma and the sample, which results in the lower emission intensity. The ablation plasma, without being cooled rapidly compared with the atmospheric pressure condition and without being expanded too much compared with vacuum condition, achieves the optimum electron temperature and density at the pressure of about 10^3 Pa , which interacts most strongly with the sample [24]. The slight increase of emission intensity at atmospheric pressure can be attributed to improved ablation efficiency from air plasma assisted heat dissipating into sample surface [33,34]. Due to the high fluence used in this experiment (676 J/cm^2), the differences between photoluminescence intensities observed at three double pulse delay values are rather small, as that can be expected from results obtained in our previous works [6,7].

The crater depth, width (full width at half-maximum of cross section profile), and volume are measured as a function of ambient pressure, as shown in Fig. 6(b)–(d). In the calculation of the depth, width and volume of a crater, the original sample surface level is used as a base line. Each data point is the averaged result of data from 3 to 5 craters. The cross section profiles of craters obtained at different pressures at zero double pulse delay are also displayed in Fig. 7. The curves of different double pulse delays in Fig. 6 follow similar trends. With increasing pressure, the crater depth

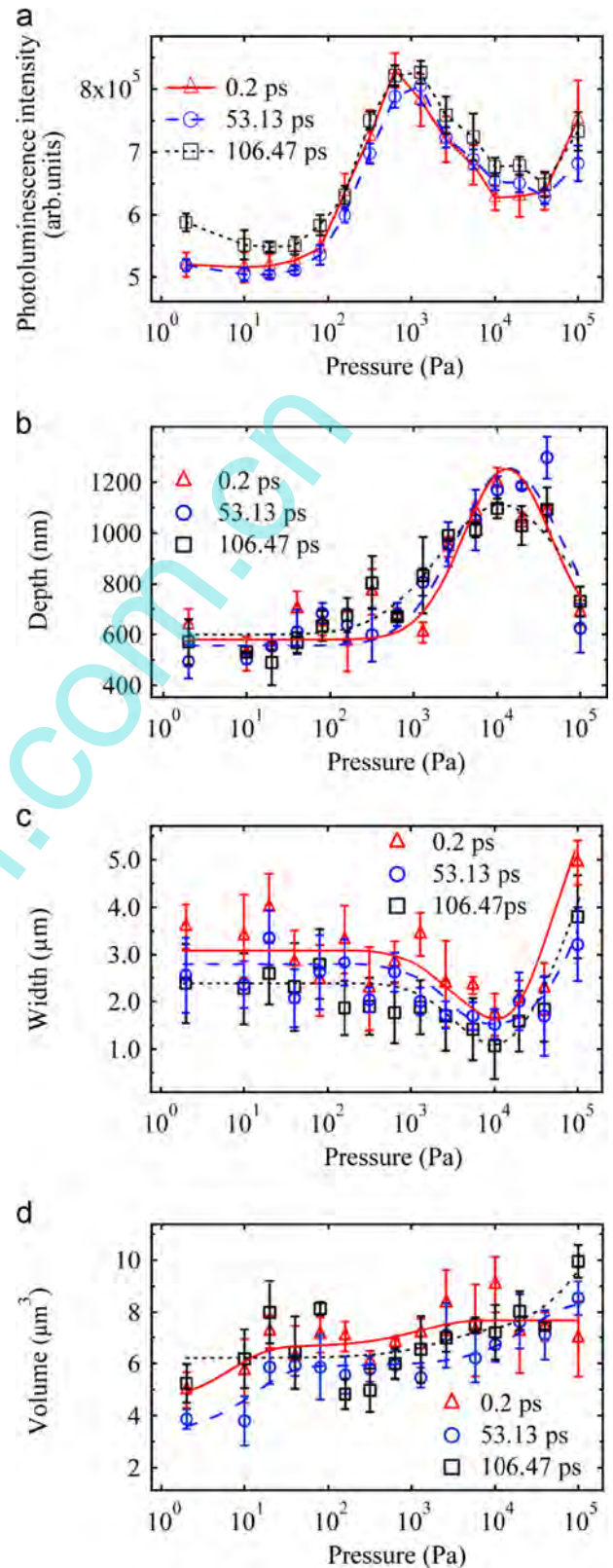


Fig. 6. (a) Photoluminescence intensity, (b) depth, (c) width and (d) volume of ablation crater as a function of ambient pressure under three double pulse delays of 0.2 ps (red triangle), 53.13 ps (blue circle) and 106.47 ps (black square), with laser fluence of 676 J/cm^2 . Solid curve, dashed curve and dotted curve correspond to 0.2 ps , 53.13 ps and 106.47 ps , respectively. Those curves in (b)–(d) are drawn to guide the eye. An average from 3 to 5 droplets is taken for each data point. (For interpretation of the references to color in this figure legend, the reader is referred to the web version of this article.)

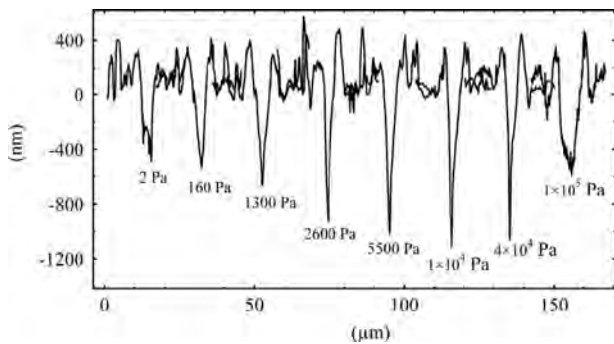


Fig. 7. Typical AFM crater cross sections obtained under different ambient pressures with laser fluence of 676 J/cm². The double pulse delay is 0.2 ps.

increases and reaches maximum around 10⁴ Pa, then decreases in even higher pressure region. The trend of width is reversed compared to that of the crater depth, the minimum is around 10⁴ Pa.

In the range of 2–10⁴ Pa, the increasing crater depth can be attributed to the greater interaction between ablation plasma and sample [24,25]. Comparing Fig. 6(a) and (b), we see that in the range of 10³–10⁴ Pa, crater depth increases while the photoluminescence intensity decreases. Though the amount of removed material and the concentration of excited species increase, the enhanced electron elastic and inelastic collisions with surrounding gas particles result in more plasma energy consumption [21,26], giving an overall decline of photoluminescence. When the ambient pressure is higher than 10⁴ Pa, the crater depth begins to decrease. This is due to two reasons. On one hand, the non-adiabatic collision process between plasma and surrounding gas consumes more plasma energy, weakening the energy coupling between plasma and sample. On the other hand, redeposited ablation material in the crater under higher pressure condition may also reduce the crater depth. Increasing the pressure, expanding plasma is not only confined in vertical direction but also in horizontal direction. Thus, the increasing or decreasing coupling between plasma and sample also results in a decreased or increased width of the crater; hence a reversed trend of width to that of depth in Fig. 6(b) and (c). The crater volume fluctuates around 6.5 μm³ over the pressure range, with a slight increasing trend as the pressure increases. The slight increase can be attributed to the assisting effect of air plasma [33,34].

The crater dimension is found to be nearly independent of pulse delay. In our previous works [6,7], we already found that crater dimension does not change much with double pulse delay. Based on other experimental evidences, the mechanisms were proposed to be: more material undergoes transitions from solid to liquid at longer double pulse delay, but most of the material resolidifies and stays in the crater without being ejected. The amount of the ejected material depends on the amount of laser energy deposited into the material, which do not change when changing double pulse delay. Other works also found similar results. For example, in the study that silver foil was ablated by femtosecond double pulse [50], it was found that the ablation crater depth from double pulse is larger than single pulse at very low laser fluence (for example, 0.65 J/cm² and 2 J/cm²), but the difference of crater depth from double pulse and single pulse is small with larger fluences (for example, 16 J/cm² and 20 J/cm²). In the current paper, we are using large fluences of 40.6 J/cm² and 676 J/cm², it can be expected that crater dimension does not change significantly with double pulse delay.

Fig. 8(a)–(d) shows some typical AFM images of craters obtained under four pressures of 40 Pa, 1300 Pa, 4 × 10⁴ Pa and

atmospheric pressure, with laser fluence of 676 J/cm². In the range of 2–1300 Pa, ablation material can eject freely from the crater compared with higher pressure condition, more droplets with irregular shapes redeposit around the ablation crater. As the pressure increases in the range of 2600–4.0 × 10⁴ Pa, a more pronounced confinement effect of the plasma takes place. Certain amount of the laser energy stored in the plasma can be transferred to the liquid layer in sample surface. Enhanced interaction produces more clear tails following the droplets. In addition, the increased pressure will prevent the ablated material ejecting from the craters, which decreases the quantity of droplets and makes the contour of crater clear. Under atmospheric pressure condition, expansion of ablation plasma is strongly limited and the cooling speed of plasma is very high. Nanometer sized tiny particles, which are formed by the resolidification of recombined material in plasma [51,52], redeposit on the sample surface [30], resulting in the blurred AFM image.

The cross sections of each droplet are analyzed and the height and full width at half-maximum are measured as a function of ambient pressure, with laser fluence of 676 J/cm², as shown in Fig. 9(a). Each data point is the averaged result of data from three droplets. The height and width values fluctuate in the pressure range. An overall increased trend of height and overall decreased trend of width are observed. This can be attributed to the enhanced interaction between ablation plasma and sample, with increasing pressure. The degree of melting increases, resulting in high temperature and larger ratio of liquid phase to solid phase in the irradiated sample. The congregated droplets with smaller width to height ratio are formed because of surface tension of liquid phase material, as discussed in Section 3.1. On the other hand, decreased energy coupling between plasma and sample under high pressure, which have been discussed in above paragraphs, may result in an increase of droplet width and decrease of height under pressures close to atmospheric pressure. This structure, however, is not observed in current experiment, probably due to the fluctuation of data.

Fig. 8(e)–(h) displays the typical AFM images of craters obtained under four pressures of 40 Pa, 1300 Pa, 4 × 10⁴ Pa and atmospheric pressure, with laser fluence of 40.6 J/cm². Liquid phase is produced after the laser radiation of the sample. In the low pressure range of 2–640 Pa, because of weaker confinement effect, the liquid material overflows freely from the crater, leaving behind an ablation crater with wider rim and irregular contour. As the pressure increases in the range of 1300 Pa to atmospheric pressure, craters with narrow rim and clear contour are observed. This is due to stronger interaction between plasma and the liquid layer, hence higher pressure in the center region of the crater. The liquid phase material is pushed out from the center, forming a clear narrow rim. A resolidified liquid structure, as shown by the arrows in Fig. 8(f)–(h), appears at the bottom of the crater. Fig. 10 shows a cross section of one crater to further illustrate the resolidified liquid structure, the edge of which is indicated by the arrows. This structure may be produced by the thermal energy coupling between plasma and liquid phase. The shapes of ablation crater and resolidified liquid structure are approximately elliptical, which has a major axis and a minor axis, as illustrated in Fig. 8(h). In order to study the size of this structure, the major axis length ratio and minor axis length ratio are plotted as functions of pressure, as shown in Fig. 9(b). Length ratio is defined as the ratio of the length of the resolidified liquid structure axis to that of ablation crater in the same direction. Both the maximum major axis length ratio and minor length axis ratio appear at the pressure of the order of magnitude of 10⁴ Pa, then decrease in even higher pressure region. Again, the increased or decreased thermal energy coupling between plasma and sample results in more or less absorbed energy into the liquid phase;

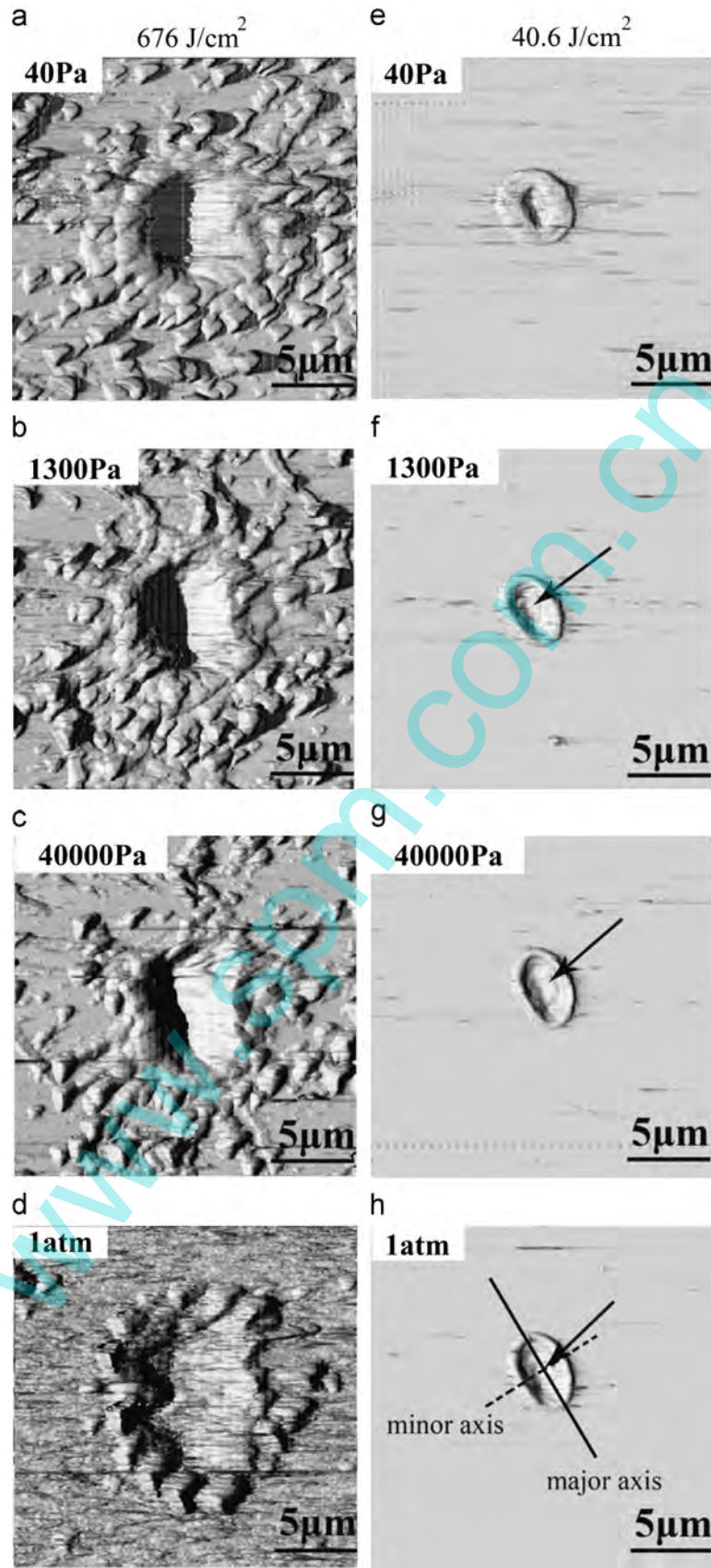


Fig. 8. AFM images of ablated craters at various ambient pressures of 40 Pa, 1300 Pa, 40,000 Pa and 1 atm (atmospheric pressure), with the double pulse delay of 0.2 ps. The laser fluences are 676 J/cm² (left column) and 40.6 J/cm² (right column). The resolidified liquid structures are shown by the arrows in (f–h). The major axis and the minor axis of the crater are illustrated by the solid line and dashed lines in (h), respectively.

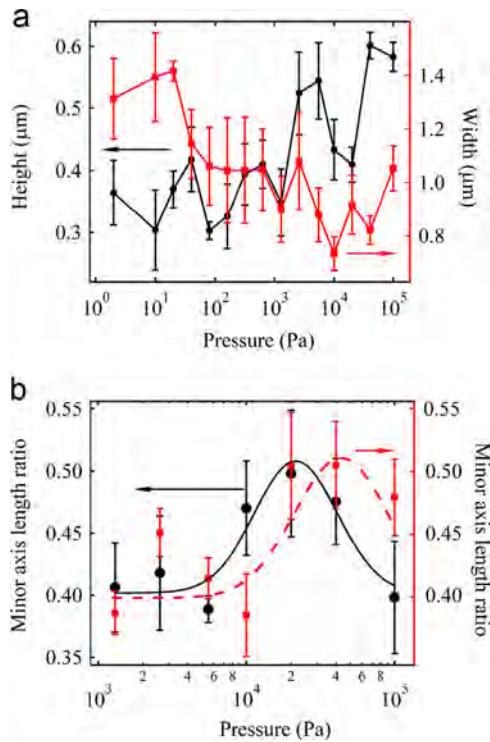


Fig. 9. (a) The average height (left axis) and width (right axis) of droplets around the crater as functions of ambient pressure, with laser fluence of 676 J/cm². (b) The minor axis length ratio (left axis) and major axis length ratio (right axis) as functions of ambient pressure, in the range of 1300 Pa to 1 atm (atmospheric pressure), with laser fluence of 40.6 J/cm². The solid curve and the dashed curve, which correspond to minor axis length ratio and major axis length ratio, respectively, are drawn to guide the eye.

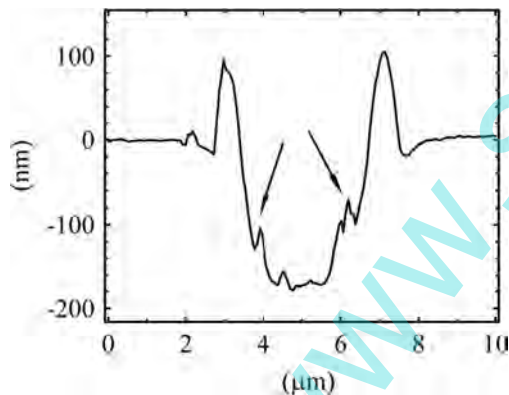


Fig. 10. AFM measured cross section of ablation crater under the pressure of 2×10^4 Pa, with laser fluence of 40.6 J/cm². The double pulse delay is 0.2 ps. The edge of resolidified liquid structure is shown by the arrows.

hence a bigger or smaller inner structure is formed due to the conduction of thermal energy.

4. Conclusion

Si is ablated by femtosecond double pulse under different experimental conditions, including double pulse delay, ambient pressure and laser fluence. Photoluminescence intensity as a function of double pulse delay shows a different trend at higher fluences compared to lower fluences, which is attributed to the combined effect of plasma reheating and laser–liquid phase interaction. The shape of the droplet is observed to be more like a thin slab at shorter double pulse delay, and more congregated at

longer delay. This result demonstrates the better energy coupling between the second laser pulse and liquid phase created by the first pulse. The higher or lower energy coupling between ablation plasma and liquid phase as well as ambient gas results in different trends of photoluminescence, crater depth and width, as functions of ambient pressure. A resolidified liquid structure inside the crater can be observed at the lowest fluence. The structure may be produced by the thermal energy coupling between plasma and liquid phase, the size change of which as a function of pressure also demonstrates that the energy coupling between plasma and liquid phase as well as ambient gas is pressure dependent.

From the results obtained in this paper, we can see that, during the ablation of silicon, splitting the energy of one laser pulse into two produces quite different behaviors. The behavior is also strongly influenced by other experimental conditions, such as fluence and ambient pressure. Depending on specific application, one might want to choose different combinations of experimental conditions. For example, to achieve higher photoluminescence intensity, as in some LIBS application, one needs to work under the pressure around 10³ Pa, choose a long double pulse delay at low laser fluence or short double pulse delay at high laser fluence. To achieve higher depth to width ratio, as in some hole drilling application, one needs to work under the pressure around 10⁴ Pa, and choose appropriate double pulse delay according to the fluence used.

This paper and many other works all reveal that the ablation process is complex, both temporally and spatially. Femtosecond double pulse is a simplified tool for studying the ablation process and controlling it. In future studies, we recommend the use of shaped femtosecond pulses, by which complete adaption of the laser field to the ablation process can be achieved. As the first step, a three pulse laser field can be used to control the ablation behavior, in which, the first pulse initiates the ablation process, the second coming after a short delay interacts with the generated plasma, and the third coming after a long delay interacts with the generated liquid phase sample.

Acknowledgment

This work is supported by the National Basic Research Program of China (973 Program) (Grant no. 2013CB922200), the National Natural Science Foundation of China (Grant nos. 10974070 and 11374124), and the Specialized Research Fund for the Doctoral Program of Higher Education, China (Grant no. 20100061110045).

References

- [1] Rethfeld B, Sokolowski-Tinten K, VonDerLinde D, Anisimov SI. Timescales in the response of materials to femtosecond laser excitation. *Appl Phys A* 2009;79:767–9.
- [2] Becker PC, Fragnito HL, Cruz CHB, Fork RL, Cunningham JE, Henry JE, et al. Femtosecond photon echoes from band-to-band transitions in GaAs. *Phys Rev Lett* 1988;61:1647–9.
- [3] Knox WH, Hirlimann C, Miller DAB. Femtosecond excitation of nonthermal carrier populations in GaAs quantum wells. *Phys Rev Lett* 1986;56:1191–3.
- [4] Liu X, Du D, Mourou G. Laser ablation and micromachining with ultrashort laser pulses. *IEEE J Quantum Electron* 1997;33:1706–16.
- [5] Smith WL. Laser induced breakdown in optical materials. *Opt Eng* 1987;17:489–503.
- [6] Singha S, Hu Z, Gordon RJ. Ablation and plasma emission produced by dual femtosecond laser pulses. *J Appl Phys* 2008;104:113520.
- [7] Hu Z, Singha S, Liu YM, Gordon RJ. Mechanism for the ablation of Si111 with pairs of ultrashort laser pulses. *Appl Phys Lett* 2007;90:131910–3.
- [8] Babushok VI, Delucia Jr. FC, Gottfried JL, Munson CA, Mizioiek AW. Double pulse laser ablation and plasma: laser induced breakdown spectroscopy signal enhancement. *Spectrochim Acta B* 2006;61:99–114.
- [9] Zeng X, Mao XL, Greif R, Russo RE. Experimental investigation of ablation efficiency and plasma expansion during femtosecond and nanosecond laser ablation of silicon. *Appl Phys A* 2005;80:237–41.

- [10] Russo RE, Mao XL, Liu C, Gonzalez J. Laser assisted plasma spectrochemistry: laser ablation. *J Anal At Spectrom* 2004;19:1084–9.
- [11] Chichkov BN, Momma C, Nolte S, von Alvensleben F, Tünnermann A. Femtosecond picosecond and nanosecond laser ablation of solids. *Appl Phys A* 1996;63:109–15.
- [12] Margetic V, Pakulev A, Stockhaus A, Bolshov M, Niemax K, Hergenröder R. A comparison of nanosecond and femtosecond laser-induced plasma spectroscopy of brass samples. *Spectrochim Acta B* 2000;55:1771–85.
- [13] Harzic RL, Huot N, Audouard E, Jonin C, Laporte P, Valette S, et al. Comparison of heat-affected zones due to nanosecond and femtosecond laser pulses using transmission electronic microscopy. *Appl Phys Lett* 2002;80:3886–8.
- [14] Semerok A, Dutouquet C. Ultrashort double pulse laser ablation of metal. *Thin Solid Films* 2004;453–454:501–5.
- [15] Ding PJ, Liu QC, Lu X, Liu XL, Sun SH, Liu ZY, et al. Hydrodynamic simulation of silicon ablation by ultrashort laser irradiation. *Nucl Instrum Methods Phys Res Sect B* 2012;286:40–4.
- [16] Pronko PP, Zhang Z, VanRompay PA. Critical density effects in femtosecond ablation plasmas and consequences for high intensity pulsed laser deposition. *Appl Surf Sci* 2003;208–209:492–501.
- [17] Zhang Z, VanRompay PA, Pronko PP. Ion characteristics of laser-produced plasma using a pair of collinear femtosecond laser pulses. *Appl Phys Lett* 2003;83:431–3.
- [18] Zhang YF, Song M, Chen C, Liu J. The role of the pressure in pulsed laser deposition of bioactive glass films. *J Non-Cryst Solids* 2008;354:4000–4.
- [19] Tull BR, Carey JE, Sheehy MA, Friend C, Mazur E. Formation of silicon nanoparticles and web-like aggregates by femtosecond laser ablation in a background gas. *Appl Phys A* 2006;83:341–6.
- [20] Juodkazis S, Okuno H, Kujime N, Matsuo S, Misawa H. Hole drilling in stainless steel and silicon by femtosecond pulses at low pressure. *Appl Phys A* 2004;79:1555–9.
- [21] Iida Y. Effects of atmosphere on laser vaporization and excitation processes of solid samples. *Spectrochim Acta B* 1990;45:1353–67.
- [22] Lee YI, Thiem TL, Kim GH, Teng YY, Sneddon J. Interaction of an excimer-laser beam with metals. Part III: the effect of a controlled atmosphere in laser-ablated plasma emission. *Appl Spectrosc* 1992;46:1597–604.
- [23] Knight K, Scherbarth NL, Cremers DA, Ferris MJ. Characterization of laser-induced breakdown spectroscopy (LIBS) for application to space exploration. *Appl Spectrosc* 2000;54:331–40.
- [24] Lobe A, Vrenegor J, Fleige R, Sturm V, Noll R. Laser-induced ablation of a steel sample in different ambient gases by use of collinear multiple laser pulses. *Anal Bioanal Chem* 2006;385:326–32.
- [25] Farid N, Bashir S, Mahmood K. Effect of ambient gas conditions on laser-induced copper plasma and surface morphology. *Phys Scr* 2012;85:015702–7.
- [26] Bashir S, Farid N, Mahmood K, Rafique MS. Influence of ambient gas and its pressure on the laser-induced breakdown spectroscopy and the surface morphology of laser-ablated Cd. *Appl Phys A* 2012;107:203–12.
- [27] Yalçın S, Tsui YY, Fedosejevs R. Pressure dependence of emission intensity in femtosecond laser-induced breakdown spectroscopy. *J Anal At Spectrom* 2004;19:1295–301.
- [28] Mateo MP, Piñon V, Anglos D, Nicolas G. Effect of ambient conditions on ultraviolet femtosecond pulse laser induced breakdown spectra. *Spectrochim Acta B* 2012;74–75:18–23.
- [29] Nakimana A, Tao H, Gao X, Hao Z, Lin J. Effects of ambient conditions on femtosecond laser-induced breakdown spectroscopy of Al. *J Phys D* 2013;46:285204–6.
- [30] Vorobyev AY, Guo CL. Enhanced energy coupling in femtosecond laser–metal interactions at high intensities. *Opt Express* 2006;14:13113–9.
- [31] Vorobyev AY, Guo CL. Direct observation of enhanced residual thermal energy coupling to solids in femtosecond laser ablation. *Appl Phys Lett* 2005;86:0011916.
- [32] Vorobyev AY, Kuzmichev VM, Kokody NG, Kohns P, Dai J, Guo CL. Residual thermal effects in Al following single ns- and fs-laser pulse ablation. *Appl Phys A* 2006;82:357–62.
- [33] Bulgakova NM, Zhukov VP, Vorobyev AY, Guo C. Modeling of residual thermal effect in femtosecond laser ablation of metals: role of a gas environment. *Appl Phys A* 2008;92:883–9.
- [34] Wu Z, Zhu X, Zhang N. Time-resolved shadowgraphic study of femtosecond laser ablation of aluminum under different ambient air pressures. *J Appl Phys* 2011;109:053113–8.
- [35] He XY, Tao J, Meng B. Analysis of graphene TE surface plasmons in the terahertz regime. *Nanotechnology* 2013;24:345203–6.
- [36] He XY, Li R. Comparison of graphene-based transverse magnetic and electric surface plasmon modes. *IEEE J Sel Top Quantum Electron* 2014;20:4600106.
- [37] He XY, Wang QJ, Yu SF. Investigation of multilayer subwavelength metallic-dielectric stratified structures. *IEEE J Quantum Electron* 2012;48:1554–9.
- [38] Theberge F, Chin SL. Enhanced ablation of silica by the superposition of femtosecond and nanosecond laser pulses. *Appl Phys A* 2005;80:1505–10.
- [39] Liu YM, Singha S, Witt TE, Cheng YT, Gordon RJ. Observation of near total polarization in the ultrafast laser ablation of Si. *Appl Phys Lett* 2008;93:161502–3.
- [40] Huber C, Orlov S, Banzer P, Leuchs G. Corrections to the knife-edge based reconstruction scheme of tightly focused light beams. *Opt Express* 2013;21:25069–76.
- [41] Bücher K, Bruns J, Wagemann HG. Absorption coefficient of silicon: an assessment of measurements and the simulation of temperature variation. *J Appl Phys* 1994;75:1127–32.
- [42] Jellison Jr. GE, Lowndes DH. Measurements of the optical properties of liquid silicon and germanium using nanosecond timeresolved ellipsometry. *Appl Phys Lett* 1987;51:352–4.
- [43] Koudoumas E, Spyridaki M, Stoian R, Rosenfeld A, Tzanetakis P, Hertel IV, et al. Influence of pulse temporal manipulation on the properties of laser ablated Si ion beams. *Thin Solid Films* 2004;372:453–4.
- [44] Choi TY, Wang HDJ, Grigoropoulos CP. Femtosecond laser induced ablation of crystalline silicon upon double beam irradiation. *Appl Surf Sci* 2002;197–198:720–5.
- [45] Spyridaki M, Koudoumas E, Tzanetakis P, Fotakis C, Stoian R, Rosenfeld A. Temporal pulse manipulation and ion generation in ultrafast laser ablation. *Appl Phys Lett* 2003;83:1474–6.
- [46] Penczak SJ, Kupfer R, Bar I, Gordon RJ. The role of plasma shielding in double-pulse femtosecond laser-induced breakdown spectroscopy. *Spectrochim Acta Part B: At Spectrosc* 2014;97:3441.
- [47] Nagli L, Gaft M, Gornushkin I. Comparison of single and double-pulse excitation during the earliest stage of laser induced plasma. *Anal Bioanal Chem* 2011;400:3207–16.
- [48] Mannion PT, Magee J, Coyne E, O'Connor GM, Glynn TJ. The effect of damage accumulation behaviour on ablation thresholds and damage morphology in ultrafast laser micromachining of common metals in air. *Appl Surf Sci* 2004;233:275–87.
- [49] Shokeen L, Schelling PK. Role of electronic-excitation effects in the melting and ablation of laser-excited silicon. *Comput Mater Sci* 2013;67:316–28.
- [50] Roberts DE, Plessis AD, Botha LR. Femtosecond laser ablation of silver foil with single and double pulses. *Appl Surf Sci* 2010;256:1784–92.
- [51] Amoroso S, Ausanio G, Bruzzese R, Vitiello M, Wang X. Femtosecond laser pulse irradiation of solid target as a general route to nanoparticle formation in a vacuum. *Phys Rev B* 2005;71:033406.
- [52] Eliezer S, Eliaz N, Grossman E, Fisher D, Gouzman I, Henis Z, et al. Synthesis of nanoparticles with femtosecond laser pulse. *Phys Rev B* 2004;69:144119–26.